

Non - peer-reviewed preprint submitted to EarthArXiv

Changes in mesophotic carbonate-platform export across the end of the last glacial cycle (Saya de Malha Bank, western Indian Ocean)

Bialik, Or M.^{1,2}; Betzler, Christian³; Braga, Juan Carlos⁴; Reijmer, John⁵; Reolid, Jesus⁴; Lindhorst, Sebastian³

1. Institute of Geology and Palaeontology, University of Münster, Corrensstr. 24, 48149 Münster, Germany
2. Dr. Moses Strauss Department of Marine Geosciences, The Leon H. Charney School of Marine Sciences, University of Haifa, Carmel 31905, Israel.
3. Institut für Geologie, Universität Hamburg, Bundesstr. 55, 20146 Hamburg, Germany
4. El Departamento de Estratigrafía y Paleontología, Facultad de Ciencias, Avenida de la Fuente Nueva S/N, 18071 Granada, Spain
5. Department of Geosciences, Faculty of Science, Vrije Universiteit Amsterdam, De Boelelaan 1085, 1081 HV Amsterdam, The Netherlands

Submitted for review in The Depositional Record

Abstract

The export of neritic material from the top of carbonate platforms is a key process in the construction of their slopes. However, our knowledge of the supply pattern of materials from platforms is dominantly based on platforms lying in the euphotic zone during the present sea-level highstand. This is a somewhat biased perspective as through geological time not all platforms were euphotic. The Saya de Malha Bank in the Mascarene Plateau is an example of a modern mesotrophic carbonate platform and as such its flooding and export patterns differ from those of euphotic ones. Using cores collected on the western slope of the Saya de Malha Bank, we explored the export patterns of the platform since the Last Glacial Maximum. Material on the platform edge is winnowed and transported to the slope by multiple possible processes. The material on the platform is a combination of high and low Mg calcite as well as high and low Sr aragonite, integrating pelagic and neritic sources. The ratio of these constituents varies over time with variation in the platform production capability as it flooded and drowned during the Holocene transgression. The material from the platform is transported in both confined flows, mainly during lowstands, and unconfined flows, mainly during late transgression and early highstand. In the present state of the highstand, supply may have diminished, leading to erosion of the canyon shoulders.

Keywords: Aragonite, High Mg calcite, Highstand shedding, Holocene, Pleistocene, SO270

Introduction

The deposits accumulated on the flanks of tropical carbonate platforms (T-factory *sensu* Schlager, 2003) are important paleoclimatic and paleoceanographic recorders. These periplatform deposits consist of pelagic material from the water column and neritic material from the shallow-water areas on top of the platform. The supply of neritic carbonate has a unique fingerprint, as it is rich in high strontium aragonite (HSA) and high magnesium calcite (HMC), and carries a unique carbon isotope signal (Bialik et al., 2020b; Schlager et al., 1994; Swart et al., 2019). These features in turn can be reflected in the observed patterns in the rock record as variations in exported HSA and HMC may impact the lithified product through differential diagenesis (Nohl et al., 2021, 2018). The supply of this neritic material is considered to occur predominantly during periods of sea-level highstand, when the platform top is flooded. Resulting deposits bear sea-level controlled variations in aragonite abundance described as "aragonite cycles" (Droxler et al., 1983; Reijmer et al., 1988; Rendle et al., 2000; Reuning et al., 2006). These mineralogical variations can be identified in recent calcareous sediments such as those of the Bahamas and Belize (Boardman et al., 1986; Gischler and Zingeler, 2002), and the Great Barrier Reef (Dunbar and Dickens, 2003). Some aragonite and HMC is lost to dissolution early in the diagenetic process (Dix and Mullins, 1988a; Sulpis et al., 2022, 2021; Swart and Guzikowski, 1988), but in the most recent deposits, the different carbonate minerals remain mostly preserved. Dissolution, however, increases porewater alkalinity and preserves the bulk carbonate mineralogy of the sediment, even beneath their lysocline (Sulpis et al., 2022). In deeper burial and geological timescales, the residual aragonite and HMC recrystallize into the more thermodynamically stable low Mg-calcite (LMC, Budd and Hiatt, 1993; Fantle and DePaolo, 2007; Melim et al., 2002). This transformation is apparent in most deep cores of carbonate platforms (Betzler et al., 2017; Eberli et al., 1997b; Shipboard Scientific Party, 1997), but is not apparent near the surface. The aragonite on the slope may be neritic HSA or pelagic low Sr-aragonite (Boardman et al., 1986), but the effect on recrystallization of the aragonite type has not been noted (Dix and Mullins, 1988b, 1988a; Mullins et al., 1985).

Export of HSA and HMC has been demonstrated in many modern active carbonate platforms with a wide active euphotic production area (Betzler et al., 2016b; Counts et al., 2019; Dunbar and Dickens, 2003; Eberli et al., 1997a; Lantzsch et al., 2007; Rendle et al., 2000; Slowey et

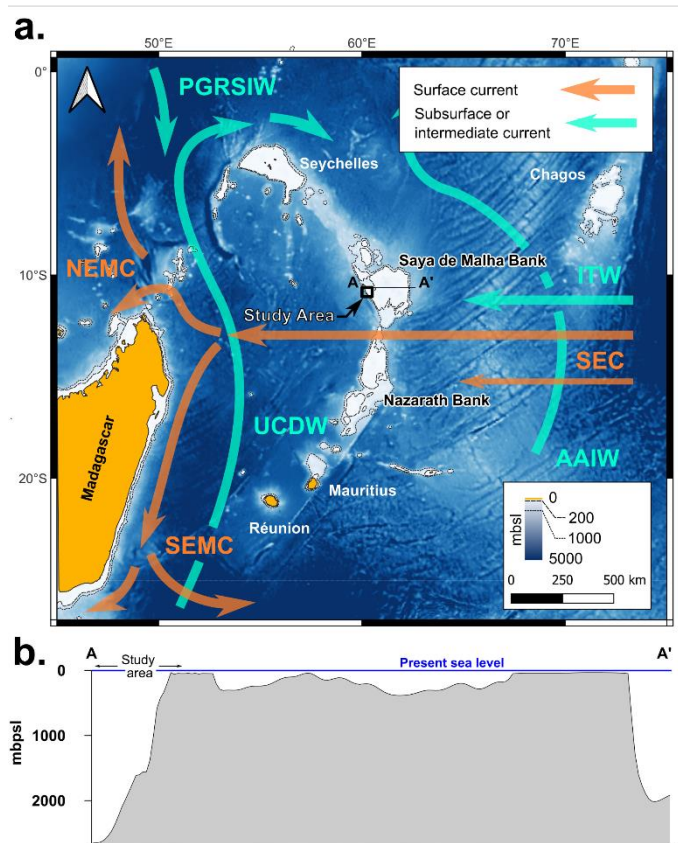


Figure 1: Location, structure and oceanography of the SMB. (A) ETOPO (Amante and Eakins, 2009) bathymetric map of the Mascarene Plateau and surrounding region with main oceanographic elements (Betzler et al., 2021; New et al., 2005). (B) section across the SMB (see (A) for location) with position of core GC59.

al., 2002). But less is known about this response on the margins of drowned platforms, i.e. carbonate platforms with a top located predominately below the euphotic depth. These platforms, currently dominantly mesophotic to aphotic, would theoretically see their euphotic production area increase during lower sea level state, with parts possibly remained submerged even in peak lowstand. With a larger production area, the potential for export would then increase during lowstand. Shallow flat-topped platforms such as the Bahamas, on the other hand, saw most of their euphotic production area emergent above sea level during glacial times. The impact of these emersions was dramatic; it is estimated that around 80% of reef areas were lost due to exposure during the glacial maximum (Kleypas, 1997) – further decreasing the export potential even during the transgression.

This work aims to test neritic production export through sea-level lowstand and highstand periods from drowned platforms and the modes of off platform transport. The target area selected is the drowned Saya de Malha platform in the western Indian Ocean. The Saya de Malha Bank (SMB) was investigated by expedition SO270 of the German research vessel RV SONNE in 2019 (Lindhorst et al., 2019), which collected sediment cores on the western (lee side) slope of the platform. Previous studies concentrated on the factors influencing the overall carbonate production (Betzler et al., 2021) and the large-scale drowning process (Betzler et al., 2023).

Geological setting

Located in the Western Indian Ocean between the Seychelles (4°S) and Mauritius (20°S), the Mascarene Plateau (Figure 1a) is the world's second largest isolated carbonate platform (about 104,510 km²). It formed since the Eocene on top of the aseismic Mascarene Ridge, which is genetically linked to the Réunion hotspot (Duncan and Hargraves, 1990; Meyerhoff and Kamen-Kaye, 1981). Geodynamically, the plateau basement represents a faulted composite arc comprising micro-continent blocks and volcanic structures (Fisher et al., 1967). The Saya de Malha Bank (SMB) is the largest of the nine carbonate banks that form the Mascarene Plateau. First described by the Percy Sladen Trust Expedition in 1905 (Rathbun, 1911), the seafloor of the SMB was sampled and mapped in detail by Soviet fishery surveys in the 1960's (Travin, 1968) and 1980's (Fedorov et al., 1980). The bank hosts a shallow submerged ring reef (8 m deep in the shallowest part, and located at an average water depth of 40 m) open to the south, a shallow lagoon (40 m – 100 m), a deep lagoon (100 m – 200 m), and an attached limestone plateau to the south in deeper waters (Fedorov et al., 1980; Vortsepneva, 2008). Following the drowning of a larger ancient platform, the modern top of SMB is located in the mesophotic depth-range and below (Betzler et al., 2023, 2021). The resulting bathymetry, from east (windward) to west (leeward) is a steep margin, followed by a narrow plateau and declining reef terraces; a basin in the centre of the bank; continuing west shallower parts are followed by an extended gentler slope (Figure 1b).

The Mascarene Plateau is bathed by the South Equatorial Current (SEC, Figure 1a) that splits and bends around the platforms (New et al., 2005). At the surface, the SEC passes across the SMB from east to west. The surface waters are nutrient-poor, tropical surface waters, which transition to less oxygenated and more nutrient-rich water across the mesophotic zone (Betzler et al., 2021; Lindhorst et al., 2019).

Methods

Data collection and sampling

All data and samples were collected as part of expedition SO270 aboard RV SONNE in September-October 2019 (Lindhorst et al., 2019). Seafloor was mapped using the ship-board Kongsberg EM122 multibeam system. Data were acquired at a cruising speed of 5.5 to 8 kn over ground by means of the hull-mounted Kongsberg EM122 multibeam systems of RV SONNE using the software Kongsberg SIS. Equidistant beam spacing was used for all lines; dual swath mode was set to dynamic, when possible, to enhance the along-track resolution. Transmit fans were stabilized for roll, pitch, and yaw. Sound-velocity profiles (SVP) and salinity profiles of the water column were obtained from conductivity-temperature-depth (CTD) probe measurements and by using XSV-02 probes (Lockheed Martin, Sippican Inc.). The software Qimera (QPS software) was used for onboard processing of multibeam data. Backscatter mosaics were rendered using the Fledermaus Geocoder Toolbox (FMGT, QPS software). All bathymetric data were corrected for astronomic tides.

Sub-bottom profiles were recorded using the ship hull mounted parametric sediment echosounder, Atlas Parasound PS70 (mk²) with the software Parastore (Teledyne RESON GmbH). The system makes use of the parametric effect caused by the interference of the two frequencies in the water column (Westervelt, 1963). The desired primary high frequency (PHF) was set to 18 kHz, the secondary low frequency (SLF) to 4 kHz. The PS70 was operated in single pulse mode with a transducer voltage of 100-120 V. Parasound data were stored in the Parasound-native formats PS3 and ASD. For processing, the PS3 data were converted to SEG-Y using the tool ps32segy (Hanno Keil, University of Bremen, Germany). Data processing was performed using the software ReflexW (Sandmeier Software) and comprises data editing, compensation for trace header delay, gain adjustment (using automatic gain control, AGC) and along-profile amplitude normalization. Time-depth conversion of Parasound data was done with a sound velocity of 1500 ms⁻¹.

Sediment core localities were selected based on seafloor mapping and sub-seafloor (Lindhorst et al., 2019). Three box-cores were collected along the edge of the platform: SO270_062-1BC (60.1503°E/10.7710°S, abbr. BC62, 99 m below present sea level - mbsl), SO270_069-1BC (60.2414°E/10.8734°S, abbr. BC69, 81 mbpsl) and SO270_070-1BC (60.2392°E/10.8733°S, abbr. BC70, 87 mbsl). Three gravity cores were also taken: gravity core SO270_059-5GC (60.0414°E/10.9257°S, recovery 5.46 m) was collected from a water depth of 2506 mbsl on the western slope of the SMB (Figures 1b, 2a); cores SO270_063-3GC (60.1662°E/10.8329°S, 697 mbsl, recovery 4.6 m) and SO270_064-5GC (60.1703°E/10.8491°S, 1275 mbsl, recovery 4.3 m) were collected from further upslope (Figure 2a). The surface sediments were also retrieved at gravity core localities using a box corer (Lindhorst et al., 2019; Betzler et al., 2023). All cores consist of unlithified sediment and were split and described on-board following the Dunham (1962) nomenclature to describe the texture. Downcore sediment color and reflectivity (L*) were measured each centimeter using a handheld Konica Minolta CM-700d color scanner. Color-scan data were calibrated and processed using the software SpectraMagic NX pro. Cores were sampled each 1 cm for grain size analysis and each 10 cm for carbonate mineralogy and stable isotope analysis.

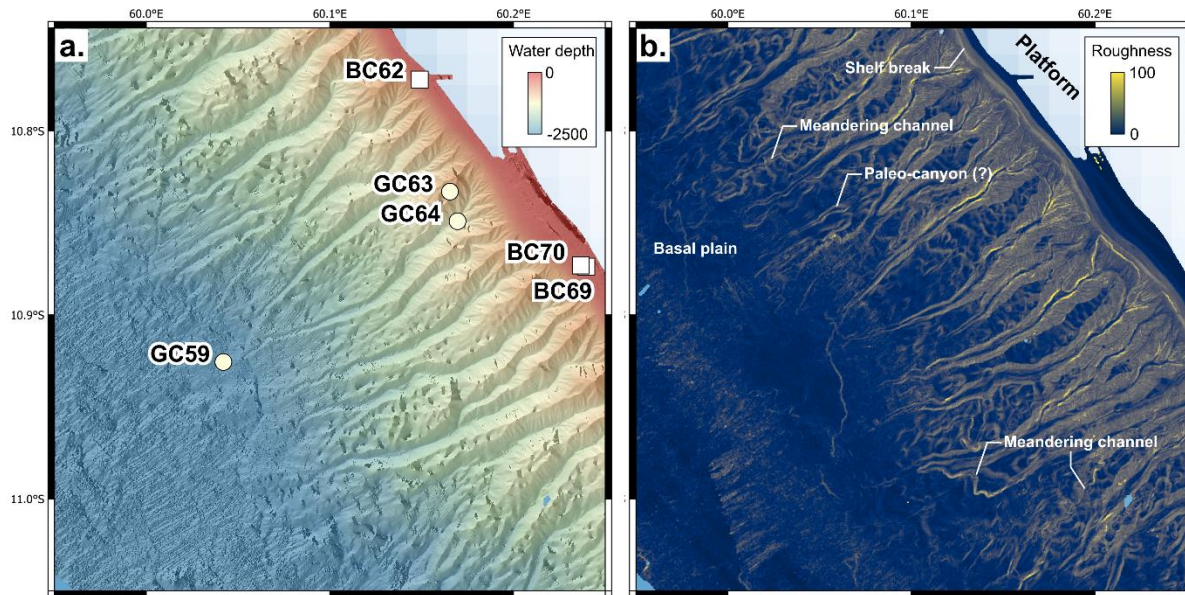


Figure 2: Detailed overview of the mapped portion on the western slope of the SMB. (A) shaded relief bathymetric map showing the locations of cores GC59, GC63, and GC64 as well as box cores BC62, BC69, and BC70. (B) roughness attribute of the map shown in a. with indicators for specific bathymetric features.

Sediment sample analysis

X-ray diffraction (XRD) analysis was carried out at the University of Haifa (Israel) using a Rigaku MiniFlex 600 benchtop XRD with a Cu source at 30 kV/10 mA from 3° to 70°, 0.05° increments by point detector. Due to the very high carbonate content, only relative ratio of the carbonate fractions (Aragonite, HMC, LMC) was determined. Fractions were calculated following the relative intensity ratio method (Hubbard and Snyder, 1988) with Rigaku PDXL software with values taken from the PDF2 database (International Centre for Diffraction Data).

Grain-size distributions were determined at the University of Hamburg (Germany) using a laser-diffraction particle-sizer (Sympatec HELOS/KF Magic; range 0.5/18 to 3,200 μm , 32 grain-size classes). Prior to measurement, bulk samples (1.5 cm^3 each) were suspended in water using tetra-sodium diphosphate decahydrate as dispersing agent. To ensure accuracy of measurements, an in-house grain-size standard was measured daily (standard deviation < 3.3 μm). Grain-size statistics are based on the graphical method (Folk and Ward, 1957), calculated using Gradistat (Blott and Pye, 2001).

Stable oxygen isotopes were analyzed at the Leibniz Laboratory for Radiometric Dating and Stable Isotope Research at the Christian-Albrechts-University zu Kiel, Germany. For this purpose, twelve specimens of the planktonic foraminifer *Globigerinoides ruber* were selected from samples each 10 cm from cores SO270_059-5GC (2506 mbsl) and SO270_063-3GC (697 mbsl), respectively. Data on grain size, stable isotopes, and carbonate mineralogy is included as supplement 1 (available online as part of: 10.6084/m9.figshare.20000396).

X-ray fluorescence core scanning

Core SO270-59-5GC was XRF scanned at the X-Ray Fluorescence (XRF) Core Scanner lab at MARUM (Bremen, Germany) using an AVAATECH series 2 core scanner with an Oxford Instruments XTF5011 X-Ray Tube 93057 and a Canberra X-PIPS Silicon Drift Detector (SDD);

Model SXD 15C-150-500). Scans were carried out at 1 cm resolution at 30 kV/1.0 mA and 10kV/0.15mA, both with 10 sec integration time. Following data quality check of processed data Br, Sr, Ca, Fe, and Si were determined to be reliable. Sr/Ca is considered here as a proxy for the flux of neritic sources HSA (Bialik et al., 2020b; Boardman et al., 1986; Counts et al., 2019; Milliman et al., 1993); Si/Fe as a proxy for the flux of biogenic silica (Bialik et al., 2020b), consisting of diatoms, radiolarian and sponge spicules – the former two being product of higher nutrient states, with implicit planktonic productivity; Br/Ca serves as a proxy for the primary productivity and the organic flux (Caley et al., 2011; Ren et al., 2009); and Fe/Ca is seen as a proxy for terrestrial flux. All XRF data is included as supplement 2 (available online as part of: 10.6084/m9.figshare.20000396).

Age model

Absolute sediment ages were constrained using calibrated ^{14}C ages (see supplement 3, 10.6084/m9.figshare.20000396) measured on foraminifer tests. Measurements were done by Beta Analytics (Florida, USA) and calibration was carried out using OxCal (v 4.4; University of Oxford) and the Marine20 calibration curve (Heaton et al., 2020). The local reservoir is unknown and therefore regarded as 0. Three radiocarbon ages were obtained from core SO270_059-5GC (abbr. GC59) and two each from SO270_063-3GC (abbr. GC63) and SO270_064-5GC (abbr. GC64). For GC59 the top of the core is assumed to represent the present, with the rest of the age model fitted based on the ^{14}C ages downcore. This age model was tested by correlating the oxygen isotope data against the LR04 global stack (Lisiecki & Raymo, 2005; see Supplementary material). Allowing for offset, the curves exhibit a good fit for the last 34 Kyr ($r=0.95$, $p<0.01$, $n=34$). A limited age model was also generated for GC63. However, an age reversal in GC64 (possibly due to reworking) did not allow to establish a robust age model of that core.

Results and interpretation

Seafloor morphology and sedimentology

Towards the western margin, the SMB retains a low angle, near flat surface until a water depth of 215 mbsl to 250 mbsl (Figures 1b; 2a). The edge of the platform is relatively flat with some platform-edge parallel features. The sediment size on the platform edge ranged between medium to coarse sand (BC62, Figure 3a, b), coarse sand (BC70, Figure 3c, d) and very coarse sand to gravel (BC69, Figure 3e, f). The sediment consists of planktonic foraminifera, small and larger benthic foraminifera, coralline algae (notably in BC69 as small rhodoliths), pteropods, octocoral sclerites, echinoid and bryozoan fragments, as well as sponge and ascidian spicules. Traces of *Halimeda* were found in BC62 and traces of scleractinians were found in BC69 and BD70.

At depth, the plateau transitions over a wide and well-defined margin into a canyon-excavated slope, separated by ridges. The ridges vary in width, from more than 1 km to several 10's of meters. The canyon heads are formed by a narrow and localized catchment, the horizontal span of the canyons average $2,612 \pm 844$ m ($n=24$). Tributaries are funneled into the main canyons at depths of around 1,400 mbsl to 1,600 mbsl. Some canyons are detached from the uppermost platform slope, possibly being abandoned paleo-canyons (Figure 2b). Canyon floors are positioned up to 500 m lower as their shoulders and channel meandering is locally present at depths exceeding 2,000 mbsl but it is not a characteristic feature of the system. Canyon courses are for the most part straight and confined, and $15,671 \pm 2,422$ m ($n=17$) long

on average. For the most part, the track of the canyons is perpendicular to the platforms edge. In some canyons, at a depth of ~1000m, the canyons channel changes directions and bends. This bending is towards the north, at times with development of meandering nature (Figure 2b). Main channels terminate at water depths of around 2,500 mbsl to 2,700 mbsl where they transfer into low relief sedimentary fans that are often amalgamated and fed by more than one canyon. Core GC59 recovered the sedimentary succession of a lobe in one of these fans.

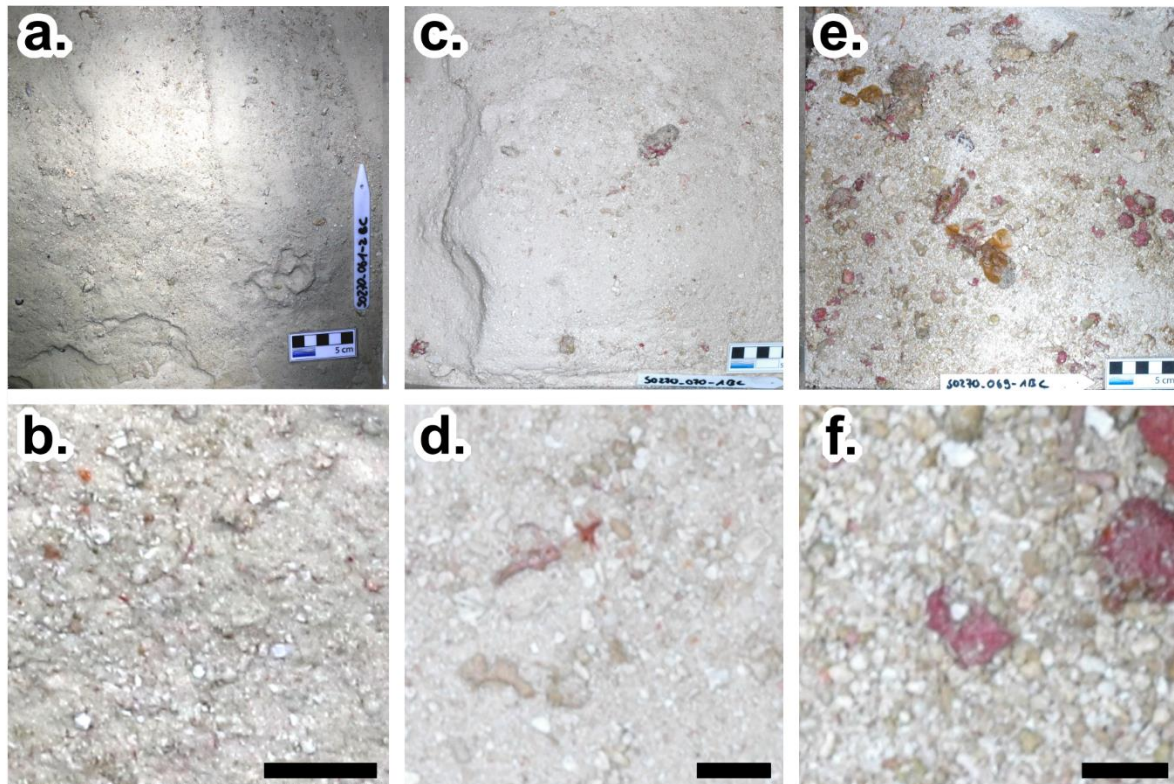


Figure 3: Photos of the box core surface (overview and closeup) for BC62 (A & B), BC70 (C & D), and BC69 (E & F). Scale card in A, C and E is 5 cm. Scale bar shown in B, D and F is 1 cm.

The platform slope has a mean inclination of 5.7° in the slope segments separating the areas excavated by the canyons (Figure 2b). The elevated, unexcavated portions of the slope exhibit an irregular surface, formed by local drainless depressions with a steep upslope termination and a gentler downslope flank. Steep steps are arcuate in shape. Core GC63 is located in one of these morphological depressions, whereas core GC64 was taken from the adjacent channel floor (Figure 2a).

Cores GC59, GC63, and GC64 capture the main depositional settings on the western slope of the SMB. The sediment of all three cores (Figure 4) is rich in carbonate mud. The sediment hosts foraminifera (dominantly planktonic) and pteropods in its sandy and coarser grained fractions. In core GC64 (canyon head), sandy layers are present, and the sand fraction is dominant in some intervals. Whereas in core GC63 (canyon shoulder) fine-grained hemipelagic material prevails. Core GC59 (basin lobe) exhibits a mixture of these two modes.

The upper half of core GC59 (down to 3.6 mbsf) is a packstone with sand-sized bioclasts being more dominant between 1.8 and 2.7 mbsf, with mudstone-wackestone and wackestone-packstone between 1.4 mbsf to 1.8 mbsf and about 2.2 mbsf to 2.4 mbsf, respectively. Between 0.1 mbsf and 0.2 mbsf and around 1.0 mbsf grainstone intervals are present;

radiolarians occur in the latter. Radiolarians were also found at 2.2 mbsf associated with a coarser-grained interval. Between 2.4 mbsf and 2.8 mbsf the mud fraction increases, and mud dominance persists as of 2.8 mbsf. From about 3.4 mbsf the sediment texture becomes dominantly wackestone to wackestone-packstone. At 1 mbsf and 2.20 mbsf some red algal debris is present. Additionally, bivalves, gastropods, larger benthic foraminifera (LBF), octocoral sclerites, echinoids, sponge and ascidians spicules were found in the upper part sampled by the box core.

Texture wise, sediment recovered by core GC63 (canyon shoulder) is a packstone until about 4 mbsf and through this interval the sand fraction decreases. The sand fraction increases again near the base of the core and packing becomes less dense. The sediment is consistently rich in carbonate mud, with the mud fraction never below 30% and being for the most part higher than 50%. The coarser material found near the base of the core consists of partially cemented unidentified allochems and pteropods. Additionally, bivalves, gastropods, octocoral sclerites, echinoids, bryozoans, serpulid fragments, and sponge and ascidian spicules were found in the upper part sampled by the box core.

The top 10 cm of core GC64 (canyon head) shows a floatstone with a few large pteropods. Further down to a depth of 2 mbsf sediment displays a wackestone with mud content increasing downcore. Between 2 mbsf and 3 mbsf the coarser fraction increases and the sediment texture transfers to a packstone. A grainstone is present between 2.60 mbsf and 2.75 mbsf, hosting radiolarians, as well as gastropod, red algal and bryozoan fragments. These coarser grains become dominant in some samples, which are free of mud. Below 3 mbsf the mud fraction becomes more dominant and the sediment texture is a wackestone with the exception of two packstone intervals between 3.4 mbsf and 3.7 mbsf. Additionally, bivalves, gastropods, LBF, octocoral sclerites, echinoids, sponge spicules, serpulid and *Halimeda* fragments were found in the upper part sampled by the box core.

Age and subdivision

Core GC59 (see supplement for age model) is divided into five main periods of regional and global significance. These being: (1) the period from the base of the core (~34 kyr BP) to the beginning of the last glacial maximum (LGM) maximum lowstand at ~26.5 kyr BP (~4.35 mbsf); (2) the period of the LGM maximum lowstand (~26.5 kyr BP to ~19.5 kyr, ~2.55 mbsf); (3) the period between the LGM maximum lowstand and the beginning of the African Humid period (AHP). at ~15.5 kyr (~1.87 mbsf); (4) the AHP itself (~15.5 to 6.5 kyr, ~0.69 mbsf); and (5) the period covering the end of the AHP to the present (Figures 5, 6). The AHP is delineated here based on sedimentological parameters and not age given the significant difference in the timing of the AHP between different sources. Mediterranean sapropel S1 duration between ~10 and ~6 kyr BP (Zirks et al., 2019), which has better age constraints, is also noted here. This event delineates a significant monsoonal activity in Eastern Africa (Rohling et al., 2015, 2002) partially conceding with the AHP and farther aid in relating regional climate to local observations.

The record in core GC63 is likely younger than 20 kyr BP (see correlation and ages in Figure 4). However, age control before 14 kyr (~3.7 mbsf) is weak and therefore we limit our analysis only to intervals 4 and 5. Unlike GC59, where oxygen isotopes could be used to help confirm the age model, in GC63 the interval was too short to fit in a satisfactory way to the global

curve. Age reversal in core GC64 (Figure 4) limits the discussion of this core only to depth. The 13.9 Ka age at 3.2 mbsf appears more reliable but is insufficient to build a reliable age model. Like core GC63, this core is also limited to intervals 4 and 5, but the position of the boundary is uncertain.

Despite these significant uncertainties, it appears that the sedimentation rate at the top of the slope (ridge and canyon head) is nearly twice as high as the canyon discharge on the plain (linear fit rate of ~ 0.14 m/kyr in core GC59, ~ 0.26 m/kyr in GC 63 and ~ 0.23 m/kyr in GC64).

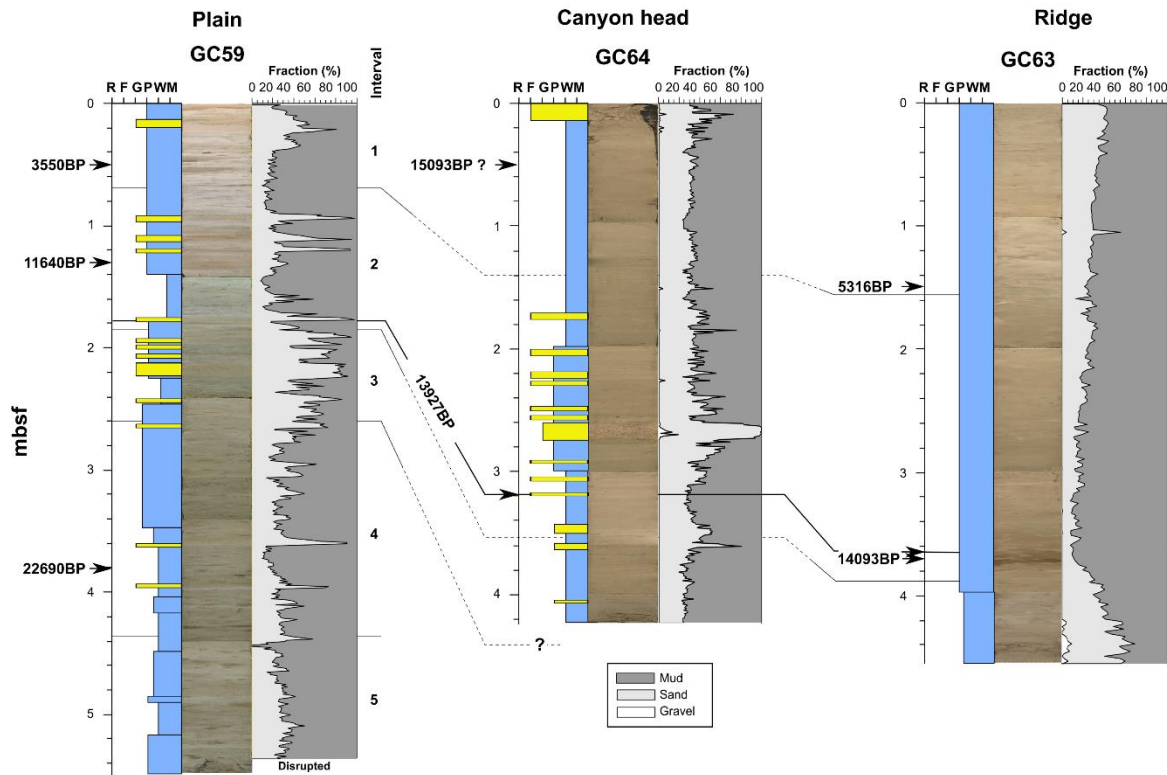


Figure 4: Columnar sections of core GC59, GC63, and GC64, showing texture, core photos, and grain size fraction for each core. Radiocarbon ages are noted by arrows with the 13.9 isochrone traced between the cores.

Detailed analysis of core SO270_059-5GC

Oxygen isotopes values (Figure 5) remain relatively stable ($\delta^{18}\text{O} \approx -0.5$ ‰) until the end of the LGM and subsequently decrease during deglaciation, stabilizing ($\delta^{18}\text{O} \approx -1.7$ ‰) between 13 kyr BP and 14 kyr BP. Planktonic foraminifer (*G. ruber*) carbon isotopes values (Figure 5) remain relatively stable ($\delta^{13}\text{C} \approx 1.0$ ‰) until about 8 kyr BP before rising and stabilizing on a higher level ($\delta^{13}\text{C} \approx 1.5$ ‰). Carbonate mineral fraction (Figure 5) remain stable with LMC being the most abundant form until the beginning of the African Humid Period at which point both HMC and aragonite content increase. HMC content begins to diminish 7 to 8 kyr BP and aragonite content diminishes in the immediate aftermath of the AHP at which point both HMC and aragonite return to their pre-AHP levels. Lightness (L^* , Figure 5) decreases to a minimum during the LGM and subsequently begins to increase. Lightness sharply increases around 10 kyr BP and remains at similar level, with a slight decline from 5 kyr BP to the present. Grain-size sorting (Figure 5) is lowest during the LGM and deglacial times, and highly variable during the AHP until about 7 Kyr BP. In the post AHP sorting exhibits a minimum and increases

towards the recent. The D_{50} (Figure 5) coarsens to a maximum in the period between the LMG and the AHP, with a few spikes also present in the LGM and AHP.

The Sr/Ca ratio (Figure 6) increases in two steps, in the aftermath of the LGM and in the beginning of the AHP, following that it displays comparable values until the present. Si/Fe (Figure 6) oscillates at around a mean value of 4.2 ± 1.0 ($n=267$) until the end of the LGM and then declines to a 2.3 ± 0.8 ($n=58$) until the beginning of the AHP at which point increase to 3.6 ± 1.7 ($n=191$) and exhibits stronger and shorter oscillation than before. Br/Ca (Figure 6) remains stable until the end of the LGM and then exhibits strong oscillation and decreases to a minimum value during the AHP, at which point it starts to increase. Fe/Ca (Figure 6) remains stable until the end of the LGM and then exhibits increased fluctuation during early deglaciation before decreasing. during the AHP, it then rises at ~9 kyr BP and remains elevated until about 3 kyr BP before dropping to a lower level. All elements exhibit a spike between 9 and 8 kyr BP (0.90 to 0.97 mbsf) which corresponds to a sand-rich (grainstone) interval.

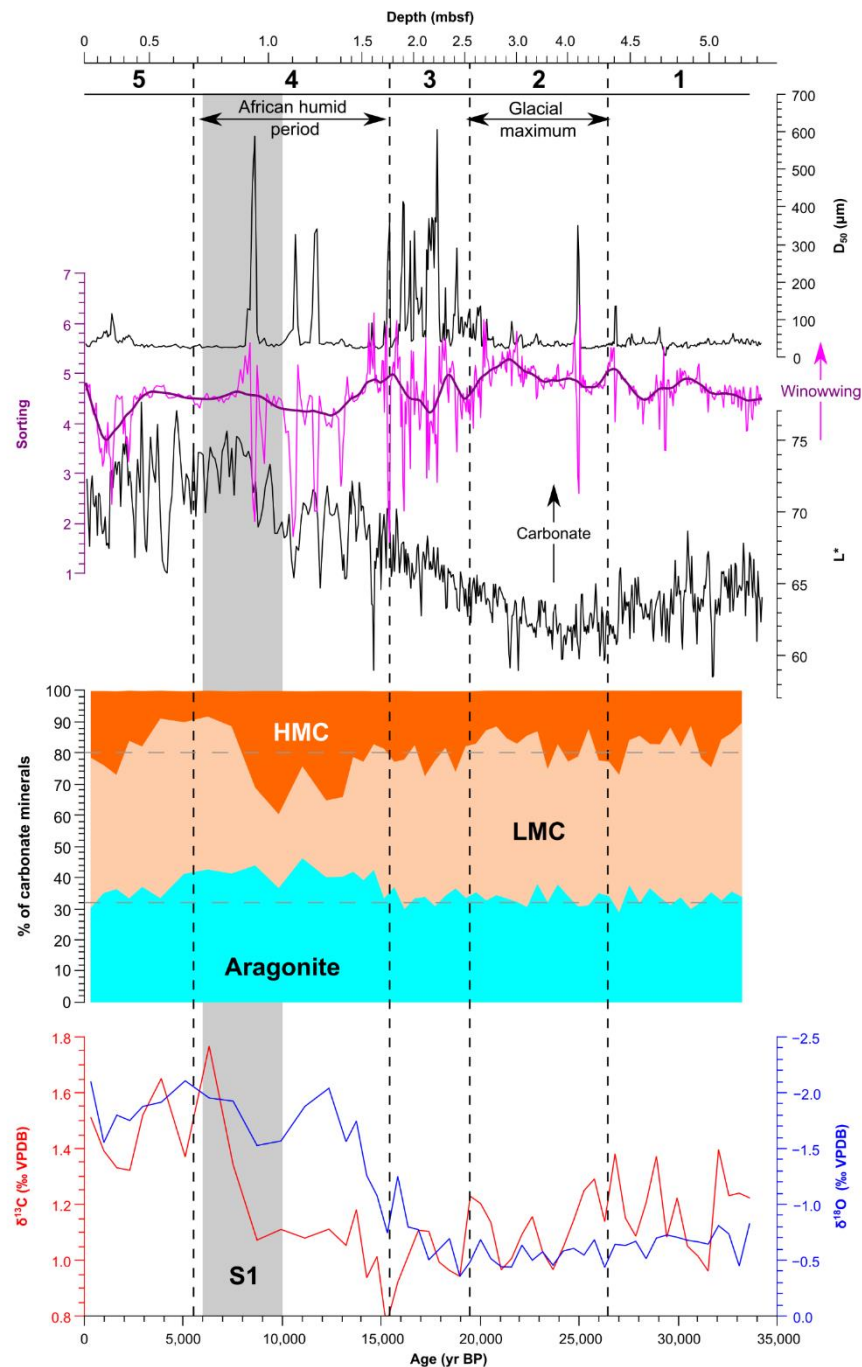


Figure 5: Temporal change in bulk stable isotopes, mineralogy, lightness and grain size parameters (sorting, D_{50}) along core GC59. Duration for the African Humid Period (deMenocal et al., 2000), Mediterranean sapropel S1 (Zirks et al., 2019) and the Last Glacial Maximum (maximum lowstand period, Clark et al., 2009) are given for discussion context.

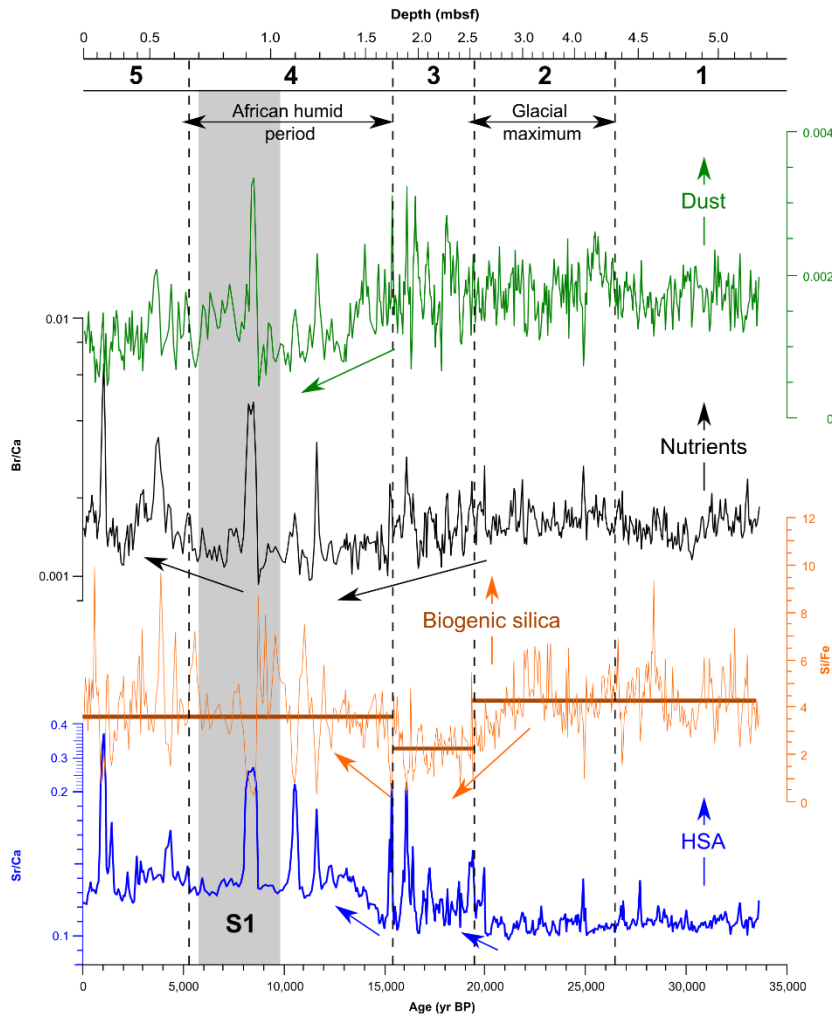


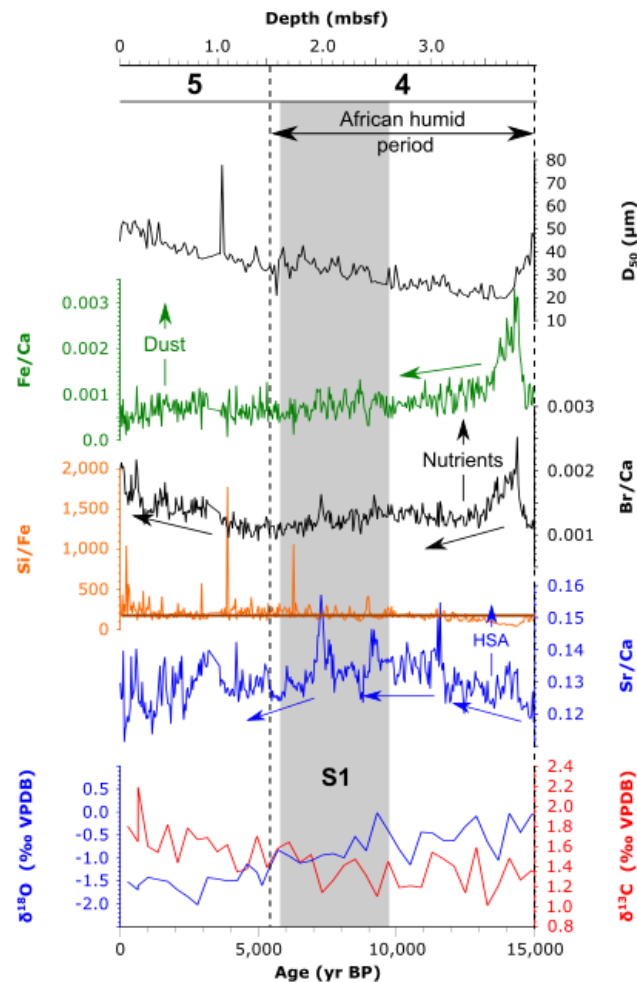
Figure 6: Temporal change in elemental ratios (Sr/Ca, Si/Fe, Br/Ca and Fe/Ca) along core GC59. Duration for the African Humid Period (deMenocal et al., 2000), Mediterranean sapropel S1 (Zirks et al., 2019) and the Last Glacial Maximum (maximum lowstand period, Clark et al., 2009) are given for discussion context.

The Sr/Ca ratio (Figure 6) increases in two steps, in the aftermath of the LGM and in the beginning of the AHP, following that it displays comparable values until the present. Si/Fe (Figure 6) oscillates at around a mean value of 4.2 ± 1.0 ($n=267$) until the end of the LGM and then declines to a 2.3 ± 0.8 ($n=58$) until the beginning of the AHP at which point increase to 3.6 ± 1.7 ($n=191$) and exhibits stronger and shorter oscillation than before. Br/Ca (Figure 6) remains stable until the end of the LGM and then exhibits strong oscillation and decreases to a minimum value

during the AHP, at which point it starts to increase. Fe/Ca (Figure 6) remains stable until the end of the LGM and then exhibits increased fluctuation during early deglaciation before decreasing during the AHP, it then rises at ~9 kyr BP and remains elevated until about 3 kyr BP before dropping to a lower level. All elements exhibit a spike between 9 and 8 kyr BP (0.90 to 0.97 mbsf) which corresponds to a sand-rich (grainstone) interval.

Detailed analysis of core SO270_063-5GC

The D_{50} is at a minimum at about 14 kyr BP with a value of 20 μm and exhibits a continued increase since then to a value of 50 μm (Figure 7). Both Br/Ca and Fe/Ca exhibit a peak at 14 kyr BP followed by a decline. This peak does not correspond to a minimum in the Ca counts indicating it does represent an increase in both Br and Fe. The Fe/Ca ratio declines onwards whereas Br/Ca exhibits a slight increase since the end of the AHP (Figure 7). Si/Fe is overall flat on a consistent value, punctuated by single intervals with very high value, likely the addition



of biogenic silica. The Sr/Ca ratio increases throughout the AHP (Figure 7), reaching a plateau before the period of Mediterranean sapropel S1 and diminishes towards the end of the AHP. As of the end of the AHP Sr/Ca overall decreases, however it is very gagged with multiple spikes of higher Sr/Ca ratio. Planktonic foraminifer (*G. ruber*) carbon isotopes exhibit an increase in value as of 8 kyr BP (~2.6 mbsf) whereas oxygen isotopes exhibit an ongoing decline through the entire period (Figure 7).

Figure 7: Temporal change in D₅₀ and elemental ratios (Sr/Ca, Si/Fe, Br/Ca and Fe/Ca) along core GC63. Oldest age restricted to 15 kyr due to temporal uncertainty in the lower part of the core. Duration for the African Humid Period (deMenocal et al., 2000) and Mediterranean sapropel S1 (Zirks et al., 2019) are given for discussion context.

Detailed analysis of core SO270_064-5GC

The D₅₀ across most of the core has a mean value of $45 \pm 10 \mu\text{m}$ ($n=402$), this near constant background level is punctuated by four coarse-grained events between ~0.09 mbsf and ~0.18 mbsf, ~1.79 mbsf and ~1.91 mbsf, ~2.61 mbsf to ~2.83 mbsf and ~3.59 mbsf and ~3.66 mbsf. These spikes consist of sand and gravel-size fractions, although the sand fraction makes up for around $37 \pm 14\%$ ($n=421$) of the total grains in the core (Figure 4).

These grain-size patterns are not well reflected in the geochemical data from the XRF scans (Figure 8). Both the Fe/Ca and Br/Ca records of core GC64 show limited variability. A local minimum in Si/Fe is present between ~2.1 mbsf and ~2.7 mbsf, corresponding partially to the largest grain-size spike, but the other spikes lack similar patterns. Sr/Ca exhibits a general increasing trend across the entire core and displays no relation to the grain-size spikes, rather showing independent peaks and troughs which do not correlate to any other record generated for this core.

Discussion

Modes and configuration of sediment transport

The western slope of the SMB, past the platform edge, consists of two architectural elements: canyons and ridges. The features present on the broader ridges (Figure 2b) are proposed to reflect downslope creeping submarine landslides. Deposits recovered in Core GC63 are primarily hemipelagic with no indications of mass transport. This absence may be partially attributed to the location being upslope and, thus, a position more likely to be eroded during mass wasting events (Pratson et al., 2000). However, the spikes in the Sr/Ca ratio (Figure 7), likely indicating introduction of neritic HSA suggest supply of fine-grained material from the platform. The absence of coarse grains suggests that the supply of neritic material takes place in unconfined low-energy flows that cannot transport such coarse material. This fine material is likely winnowed from the platform.

The sediment on the platform edge

(Figure 3) is rather coarse grained, without a significant fine fraction, suggesting active, although possibly intermittent, winnowing. Three possible processes may facilitate this winnowing: deep storm waves, internal waves, and bottom currents. The tropical Indian Ocean is prone to tropical cyclones, with over ten significant cyclones making landfall on the southeastern African margin per year (Mavume et al., 2010). These cyclones come around the SMB from the east and would push material to the west. However, it is unclear how deep the associated waves could impact the seafloor. During cyclone events in the northwestern Indian Ocean, the common wave frequency was measured to be around 0.1 Hz (Sirisha et al., 2015), which would equate to a wavelength of ~156 m – and a wave base of ~78m. This could be a viable mechanism to transport fine material to depth through hyperpycnal flows (Bialik et al., 2022). But it is not deep enough to scour the seafloor at a depth exceeding 200 m, where the platform margin resides on the western edge. Individual waves may impact at that depth, but the effect of such waves is unclear. Internal waves have been observed on the SMB and their impact documented (Betzler et al., 2023). They are impactful at the depth of the platform edge on the west and can winnow and remobilize sediment. These waves would originate from the south and propagate northwards along the edge of the shelf. Elevated flow velocities have been documented on the western edge of the SMB in comparable depth (Lindhorst et al., 2019), which may be the propagation of these internal waves or bottom currents. At this time, it is not possible to deconvolve these two elements.

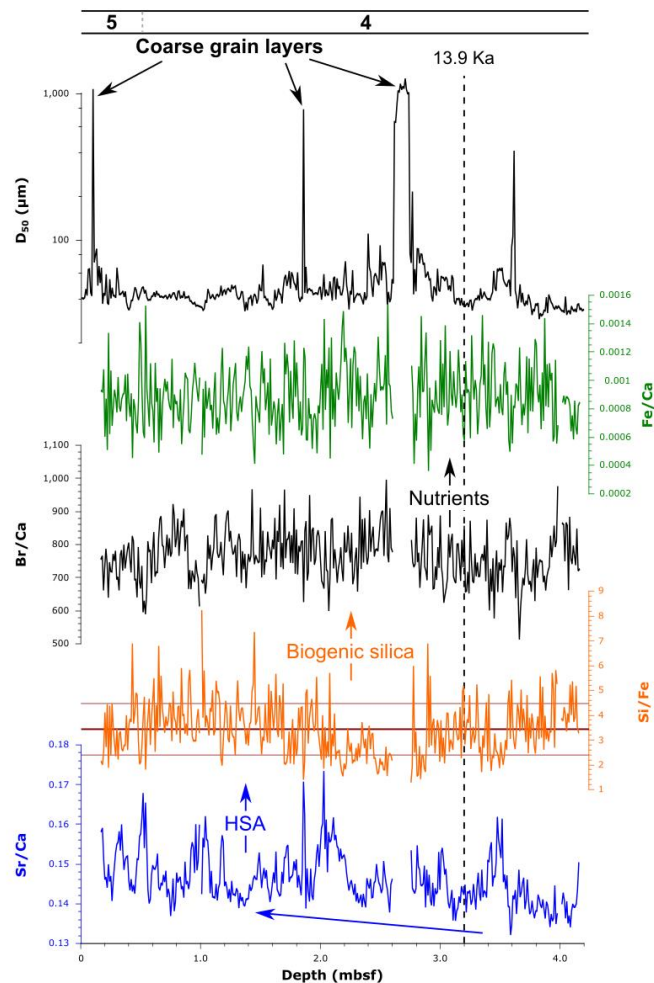


Figure 8: Temporal change in D50 and elemental ratios (Sr/Ca, Si/Fe, Br/Ca and Fe/Ca) along core GC64. Note that this core is displayed only in depth.

Coarse-grained intervals in both the canyon head (core GC64) and the mouth of the canyon (core GC59) indicate transport in and into the canyon through high-energy focal flows. The presence of neritic components (red algae, LBF, *Halimeda*) indicates that these sites receive material from the platform. The supply of neritic material and occurrence of coarse-grained intervals intercalated with fine-grained ones suggest transport by episodic high-energy grain flows, driven, perhaps, by major tropical storms. It cannot be excluded that some of this material was eroded from the canyon wall, which may be the source of the older material near the top of core GC64.

The higher sedimentation rate during the Holocene high sea-level state (highstand) on the canyon flank relative to the canyon head suggests that the less-confined transport mode is common. There is no evidence that the canyons are laterally filled. Where a canyon becomes detached from its upslope or downslope elements, it is usually due to the activity of an adjacent canyon (Figure 2b). The lower sedimentation rate in the channel and presence of coarse-grained material (Figure 4, core GC63) suggests that transport and winnowing in the conduit continues during a highstand in sea level.

The better sorting, indicative of winnowing, on the basal plain during the glacial maximum (Figure 5) with low sea-level (lowstand) suggests some level of persistent transport energy winnowing the fine pelagic input. This transport process may be lateral or downslope, with present evidence insufficient to distinguish between the modes of transport. In the early deglaciation, however, the strong oscillations in both grain size and sorting suggest intermittent events indicating episodic transport as sediment gravity flows rather than the action of persistent currents. The higher frequency of such events and higher overall sorting during the lowstand (Figure 5), points to an increase in high-energy downslope transport, probably through the canyons.

Changes in accumulation patterns and controls

Examining the various variations in the cores, a temporal pattern of changes in oceanographic conditions and associated supply of material from the platform emerges. During the LGM and the period preceding it (intervals 1 and 2), neritic export was low as evidenced by both the Sr/Ca ratio and the lower amount of both aragonite and HMC. At the base of the slope (Figure 5) sorting and winnowing were the strongest during the LGM itself, as nutrient and neritic export were likely at their peak. The grain distribution may be due to either downslope or slope parallel flow. Biogenic silica during the LGM and preceding period was higher overall and so was dust supply. The minimum in lightness during this period (presetting less carbonate and more organic matter / terrestrial material, Poli et al., 2010) similarly support this interpretation.

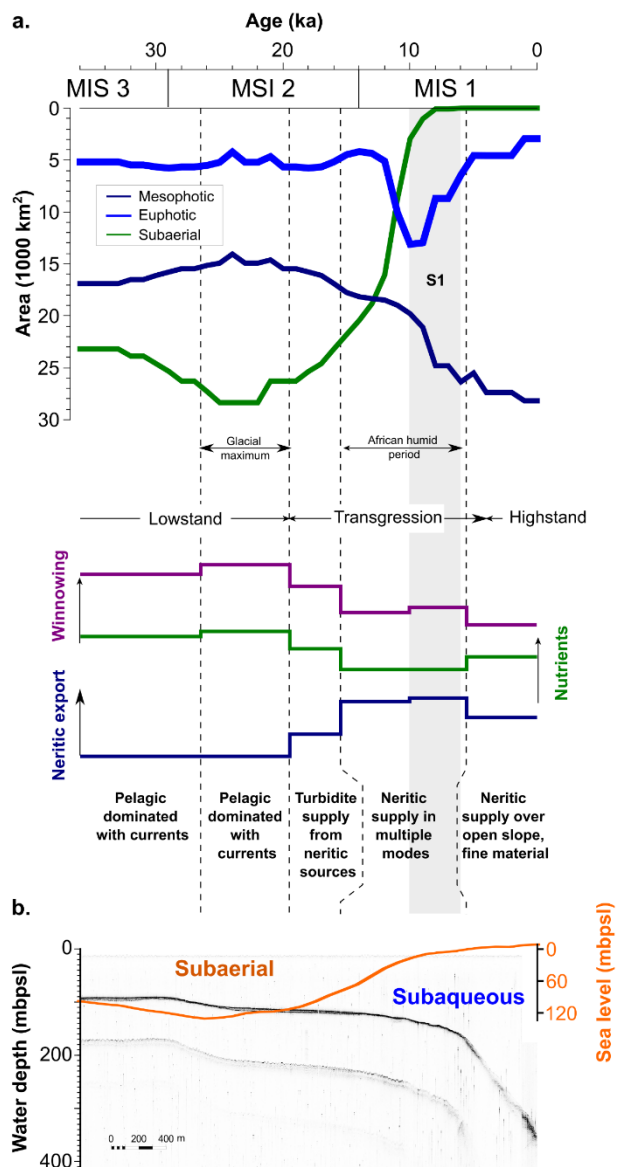
In the aftermath of the LGM (interval 3), the exposed land area on the SMB decreased, leading to an increase in the mesophotic (30 to 150 m) production area (Figure 9a). With this shift, neritic supply increased as biogenic silica supply declined. The supply of neritic material downslope was in pulses and localized, indicated by the strong oscillation in sorting and peaks in grain size, likely indicating sediment gravity flows (Figure 9b). The inconsistency in the Fe/Ca ratio between the plain (GC59) and the ridge (GC63) could be due to different dispersal patterns, but alternatively could be related to monsoonal wind intensity and associated dust influx. The SMB is an isolated, open-ocean carbonate platform, situated far from potential fluvial input (Figure 1a). With ocean currents from the east, i.e. from the open Indian Ocean,

and the westward-directed atmospheric circulation of the trade wind belt, we consider terrestrial input as minor and primarily derived from aeolian dust (Léon and Legrand, 2003). That said, the increase in both Br/Ca and Fe/Ca without any depletion in Ca, would suggest that productivity is paired with dust. Dust can play an important part in fertilization of isolated carbonate platforms (Swart et al., 2014). There are two possible dust source to the SMB, the Middle East and Australia (Kok et al., 2021), both thousands of kilometers away. The significant transport distance from likely dust sources suggests the supply was probably highly limited and as such the spatial pattern of atmospheric distribution might be stochastic, limited to events rather than constant supply, and not uniformly spread across the SMB. Some uncertainties do persist given the unknown regarding the provenance of the material on the platform which may introduce phase lags (Emmermann, 2000).

Figure 9: (A) Changes in the relative areas of production on the SMB over the period recorded in core GC59 (calculated from GEMCO bathymetric data and sea level reconstruction by Spratt and Lisiecki, 2015) and corresponding reconstruction of conditions as recorded in the core. (B) Parasound line across the western flank of the SMB (Lindhorst et al., 2019) showing the form of the seafloor at the platform edge in the study area, overlay by the sea level curve (Spratt and Lisiecki, 2016; X axis as in A).

During the first half of the AHP (interval 4), land area on the SMB had significantly reduced (Figure 9a), leading to expansion of mesophotic areas first and then of euphotic production areas. During this period, HMC export increased significantly (Figure 5) as did over all aragonite supply, with Sr/Ca ratios indicating this aragonite to be neritic HSA. This supply was not localized to higher density flows in the canyons but had to be in unconfined flows (Figure 9b), as the Sr/Ca ratio peaks on the ridge (Figure 7) and in the mouth of the canyon (Figure 6), but not in the canyon head (Figure 8). Although HMC forms in both the euphotic zone and the mesophotic zone, the organisms producing it (notably soft body corals and calcareous red

algae) are more common in mesophotic depths (Benayahu et al., 2019; Grossowicz and Benayahu, 2015; Perrin et al., 1995; Yesson et al., 2012). The flux of aragonite and HMC suggest that supply in the first half of the AHP was predominantly from the mesophotic zone. With the onset of the insolation maxima (bracketed here by Mediterranean sapropel S1) the



euphotic area on the SMB reached its apex (Figure 9). Monsoonal intensity was at its peak between 8 kyr and 6 kyr (de Menocal, 2015), corresponding to the apexes of Mediterranean sapropel S1 (Zirks et al., 2019). This intensification was driven by insolation and corresponds to stronger winds and evaporation in the tropics (Zhao et al., 2005) with maximum expansion of the ITCZ and monsoonal extension (Ziegler et al., 2010). These climatic changes should correspond to maximum intensity of the western Indian Ocean jet system and upwelling systems (Murtugudde et al., 2007; Prell, 1984; Prell and Campo, 1986). The increase in $\delta^{13}\text{C}$ values of the planktonic foraminifera during this time (Figures 5, 7) is dissimilar to the patterns observed in benthic foraminifera (Raymo et al., 1990), suggesting it was likely the product of changes in the surface carbon budget. This shift might be the result of warming-induced degassing of CO_2 (Sisma-Ventura et al., 2017) or a shift in productivity.

In the aftermath of the AHP (interval 5) and the beginning of the Holocene highstand, sea level nearly reached its current level (Spratt and Lisiecki, 2015). With this high sea-level state, most of the SMB became mesophotic (Figure 9a). The rapid increase in sea level (Figure 9b) likely exceeded the vertical growth rate the reefs established following the transgression. Limited preexisting topography elevated to modern euphotic depth meant that reefs and other buildups established on the deep substrate could not keep up. It is unclear if additional factors, such as upwelling or turbidity, were at play during this critical time. Would they have, it is possible they would also suppress the growth rate, limited keep up on larger regions. At the transition to the post AHP, oxygenation began to deteriorate and primary productivity to increase, although the latter and dust supply diminished around ~3 kyr BP in cores GC59 and GC63 (Figures 5, 6), suggesting some Meghalayan (late Holocene) weakening of winds. However, this shift in Fe/Ca is not present in the canyon head (core GC64), indicating that this signal may also have other controlling parameters. The supply of less oxygenated waters increased with the Meghalayan expansion of the western Indian Ocean OMZ (Gaye et al., 2018). While aragonite content in core GC59 diminishes after the AHP (Figure 5), Sr/Ca ratio does not (Figure 6), suggesting that the decline was mainly in LSA from pelagic sources. The lightness of core GC59 decreases during this period, overall indicating decline in the carbonate content, which corresponds to some increase in nutrients. Sorting decreases during this period, marking a decline in high-energy processes (current and/or downslope transport) and winnowing of sediment. Likely there also was a shift in the mode of aragonite supply as the Sr/Ca on the ridge diminished (Figure 7) and increased in the canyon (Figure 8). This may indicate more reworking of material from the canyon walls into it at this time. The combined effect would suggest reduction in sediment supply from the platform at that time. This decrease may have several reasons, including the diminishing production with the transition to mesophotic communities, the weakening of storm grazing with in the aftermath of the AHP, reduced interaction with the SEC at depth or some shift in nutrients.

Controls and implications

The western Indian Ocean has seen fundamental shifts in its oceanographic controls over geological scale, governed by climate and atmospheric configuration (Betzler et al., 2016a; Bialik et al., 2020a; Gurlan et al., 2008). Within the Pleistocene to Holocene, atmospheric, oceanic and sea-level changes have had a fundamental sway. Their influence most notably is reflected in the export and distribution patterns of sediment derived from carbonate platforms (Betzler et al., 2015, 2013; Counts et al., 2021; Jorry et al., 2020, 2016; Paul et al., 2012). The complicated relationships among controlling factors are evident in the SMB. In euphotic platforms, downslope supply is dominated by winnowing of the platform top during highstands (Counts et al., 2019; Schlager et al., 1994). The case in the SMB, however, is more

complicated with the transition from deeper currents at the base of the platform during the lowstand, increase in focused supply during the transgression, and finally highstand shedding. The significant span of a deeper water region on the SMB allows for persistent euphotic and mesophotic production through the entire glacial cycle, being most abundant in the late transgression rather than during the highstand (Figure 10). The SMB continued to export aragonite despite the significant reduction in the euphotic area with the transition to the highstand, suggesting that dominant factories have shifted along that transition. It is not entirely clear why exactly did neritic carbonate production did not keep up with sea level during the transgression. It was suggested that the maximum growth rate of a euphotic reef is around 12.5 mm/year (Bosscher and Schlager, 1992), the maximum sea level rise rate during the Holocene transgression in the region may have been around 6.5 mm/year (Camoin et al., 1997), suggesting accumulation could have kept up. However, global compilations (Spratt and Lisiecki, 2016) suggest periods (notably between 12 and 13 kyr) where the rate of sea level rise exceeded 15 mm/year. Yet here this is a period marked by high export of neritic material (Figures 5, 6 & 7). Other factors must, therefore, be also invoked such as lower growth rate, either due to temperature or nutrient state.

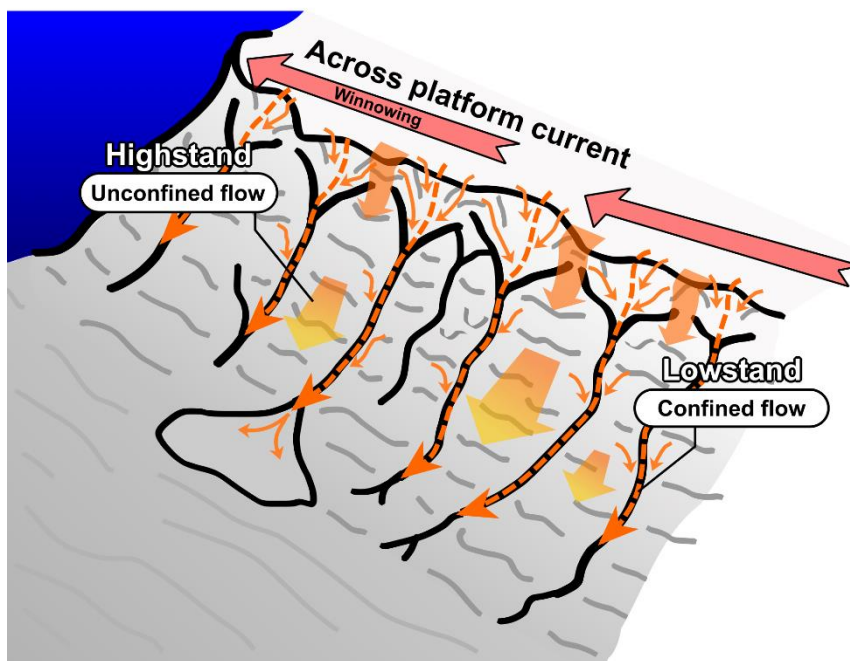


Figure 10: Conceptual model for modes of transport along the western slope of the SMB.

In euphotic carbonate platforms, the role of wind and nutrients have been also invoked to modulate neritic production (Reijmer and Andresen, 2007; Turpin et al., 2011). It is therefore possible that some of the glacial/interglacial variations observed here are also the product of the reorganization of the winds and nutrient regime in the area with post-glacial warming, affecting nutrients limitations.

Conclusions

The Mascarene Plateau is an mesophotic carbonate platform situated in the tropical zone, being mostly drowned. As such, its response to sea-level changes is somewhat different from that of other carbonate platforms. Material is driven and sloughed from the platform through a combination of storm events, bottom currents, and internal waves. These processes induce both the resuspension of fine material in distributed flow and confined grain flows. Material transport from the platform was preferentially confined during the lowstand associated to the Last Glacial Maximum, and became unconfined towards the end of the Holocene

transgression. With the transition to the modern highstand, the supply diminished. The diminishing sediment supply likely led to erosion of the canyon walls due to sediment starvation. The water depth of the platform likely plays a role in the specific transport mechanism through the mode of material production on the platform, depth of internal wave interface, storm wave base depth relative to platform depth and bottom current configuration.

Data availability

All data and supplements are available online via the FigShare repository as 10.6084/m9.figshare.20000396 and available prior to publication through: <https://figshare.com/s/cdaf396b545a38bd0e55>.

Acknowledgements

We acknowledge outstanding support by the Master and crew of RV SONNE and by the shipboard scientific party. The research cruise SO270 and post-cruise work was funded by the Bundesministerium für Bildung und Forschung (BMBF, Germany; grant 03G0270A to CB). The Joint Commission of the Extended Continental Shelf Mascarene Plateau Region is thanked for allowing work in the Mascarene Joint Management Area (JMA) and the Department for Continental Shelf, Maritime Zones Administration & Exploration (Mauritius) for allowing work in the EEZ of the Republic of Mauritius. Jutta Richarz is thanked for grain-size analyses. OMB was supported by Marie Skłodowska Curie fellowship 101003394 (RhodoMalta) during post-cruise work. JR was supported by Ministerio de Ciencia e Innovación of the Spanish Government through the Ramón y Cajal project RYC2021-034362-I. JR and JCB thanks research group RNM-190.

References

- Amante, C., Eakins, B.W., 2009. ETOPO1 arc-minute global relief model: procedures, data sources and analysis. Boulder, Colorado.
- Benayahu, Y., Bridge, T.C.L., Colin, P.L., Liberman, R., McFadden, C.S., Pizarro, O., Schleyer, M.H., Shoham, E., Reijnen, B.T., Weis, M., Tanaka, J., 2019. Octocorals of the Indo-Pacific, in: Loya, Y., Puglise, K., Bridge, T. (Eds.), *Mesophotic Coral Ecosystems. Coral Reefs of the World*, vol 12. Springer, pp. 709–728.
https://doi.org/10.1007/978-3-319-92735-0_38
- Betzler, C., Eberli, G.P., Alvarez Zarikian, C.A., Alonso-García, M., Bialik, O.M., Blättler, C.L., Guo, J.A., Haffen, S., Horozal, S., Inoue, M., Jovane, L., Kroon, D., Lanci, L., Laya, J.C., Ling Hui Mee, A., Lüdmann, T., Nakakuni, M., Nath, B.N., Niino, K., Petruny, L.M., Pratiwi, S.D., Reijmer, J.J.G., Reolid, J., Slagle, A.L., Sloss, C.R., Su, X., Swart, P.K., Wright J.D., Y., Z., Y., 2017. Site U1467. *Proc. Int. Ocean Discov. Progr.* 359.
<https://doi.org/10.14379/iodp.proc.359.105.2017>
- Betzler, C., Eberli, G.P., Kroon, D., Wright, J.D., Swart, P.K., Nath, B.N., Alvarez-Zarikian, C.A., Alonso-García, M., Bialik, O.M., Blättler, C.L., Guo, J.A., Haffen, S., Horozal, S., Inoue, M., Jovane, L., Lanci, L., Laya, J.C., Mee, A.L.H., Lüdmann, T., Nakakuni, M., Niino, K., Petruny, L.M., Pratiwi, S.D., Reijmer, J.J.G., Reolid, J., Slagle, A.L., Sloss, C.R., Su, X., Yao, Z., Young, J.R., 2016a. The abrupt onset of the modern South Asian Monsoon winds. *Sci. Rep.* 6, 29838. <https://doi.org/10.1038/srep29838>
- Betzler, C., Hübscher, C., Lindhorst, S., Lüdmann, T., Reijmer, J.J.G., Braga, J., 2016b. Lowstand wedges in carbonate platform slopes (Quaternary, Maldives, Indian Ocean). *Depos. Rec.* 2, 196–207. <https://doi.org/10.1002/dep2.21>
- Betzler, C., Lindhorst, S., Lüdmann, T., Reijmer, J.J., Braga, J.-C., Bialik, O.M., Reolid, J., Eisermann, J.O., Emeis, K., Rixen, T., Bissessur, D., 2021. Current and sea level control the demise of shallow carbonate production on a tropical bank (Saya de Malha Bank, Indian Ocean). *Geology* 49, 1431–1435. <https://doi.org/10.1130/G49090.1>
- Betzler, C., Lindhorst, S., Lüdmann, T., Weiss, B., Wunsch, M., Braga, J.C., 2015. The leaking bucket of a Maldives atoll: Implications for the understanding of carbonate platform drowning. *Mar. Geol.* 366, 16–33.
<https://doi.org/10.1016/j.margeo.2015.04.009>
- Betzler, C., Lindhorst, S., Reijmer, J.J.G., Braga, J.C., Lüdmann, T., Bialik, O.M., Reolid, J., Geßner, A., Hainbucher, D., Bissessur, D., Braga, J.C., Reijmer, J.J.G., Reolid, J.,
- Bialik et al., Mesophotic post-glacial carbonate-platform export patterns

- Geßssner, A.-L., Hainbucher, D., 2023. Carbonate platform drowning caught in the act: The sedimentology of Saya de Malha Bank (Indian Ocean). *Sedimentology* 70, 78–99. <https://doi.org/10.1111/sed.13032>
- Betzler, C., Lüdmann, T., Hübscher, C., Fürstenau, J., 2013. Current and sea-level signals in periplatform ooze (Neogene, Maldives, Indian Ocean). *Sediment. Geol.* 290, 126–137. <https://doi.org/10.1016/j.sedgeo.2013.03.011>
- Bialik, O.M., Auer, G., Ogawa, N.O., Kroon, D., Waldmann, N.D., Ohkouchi, N., 2020a. Monsoons, Upwelling, and the Deoxygenation of the Northwestern Indian Ocean in Response to Middle to Late Miocene Global Climatic Shifts. *Paleoceanogr. Paleoclimatology* 35, 1–17. <https://doi.org/10.1029/2019PA003762>
- Bialik, O.M., Bookman, R., Elyashiv, H., Marietou, A., Saar, R., Rivlin, T., Taha, N., Benaltabet, T., Lotem, N., Funaro, E., Antler, G., 2022. Tropical storm-induced disturbance of deep-water porewater profiles, Gulf of Aqaba. *Mar. Geol.* 453, 106926. <https://doi.org/10.1016/j.margeo.2022.106926>
- Bialik, O.M., Reolid, J., Betzler, C., Eberli, G.P., Waldmann, N.D., 2020b. Source shifts to periplatform deposits during the early to middle Miocene in response to climatic and oceanographic forcing, Maldives, western Indian Ocean. *Palaeogeogr. Palaeoclimatol. Palaeoecol.* 559, 109969. <https://doi.org/10.1016/j.palaeo.2020.109969>
- Blott, S.J., Pye, K., 2001. GRADISTAT: a grain size distribution and statistics package for the analysis of unconsolidated sediments. *Earth Surf. Process. Landforms* 26, 1237–1248. <https://doi.org/10.1002/esp.261>
- Boardman, M.R., Neumann, A.C., Baker, P.A., Dulin, L.A., Kenter, R.J., Hunter, G.E., Kiefer, K.B., 1986. Banktop responses to Quaternary fluctuations in sea level recorded in periplatform sediments. *Geology* 14, 28–31. [https://doi.org/10.1130/0091-7613\(1986\)14<28:BRTQFI>2.0.CO;2](https://doi.org/10.1130/0091-7613(1986)14<28:BRTQFI>2.0.CO;2)
- Bosscher, H., Schlager, W., 1992. Computer simulation of reef growth. *Sedimentology* 39, 503–512. <https://doi.org/10.1111/j.1365-3091.1992.tb02130.x>
- Budd, D.A., Hiatt, E.E., 1993. Mineralogical Stabilization of High-magnesium Calcite: Geochemical Evidence for Intracrystal Recrystallization Within Holocene Porcellaneous Foraminifera. *J. Sediment. Res.* 63, 261–274. <https://doi.org/10.1306/D4267AD7-2B26-11D7-8648000102C1865D>
- Caley, T., Malaizé, B., Zaragosi, S., Rossignol, L., Bourget, J., Eynaud, F., Martinez, P., Giraudeau, J., Charlier, K., Ellouz-Zimmermann, N., 2011. New Arabian Sea records
- Bialik et al., Mesophotic post-glacial carbonate-platform export patterns

- help decipher orbital timing of Indo-Asian monsoon. *Earth Planet. Sci. Lett.* 308, 433–444. <https://doi.org/10.1016/j.epsl.2011.06.019>
- Camoin, G.F., Colonna, M., Montaggioni, L.F., Casanova, J., Faure, G., Thomassin, B.A., 1997. Holocene sea level changes and reef development in the southwestern Indian Ocean. *Coral Reefs* 16, 247–259. <https://doi.org/10.1007/s003380050080>
- Clark, P.U., Dyke, A.S., Shakun, J.D., Carlson, A.E., Clark, J., Wohlfarth, B., Mitrovica, J.X., Hostetler, S.W., McCabe, A.M., 2009. The Last Glacial Maximum. *Science* (80-). 325, 710–714. <https://doi.org/10.1126/science.1172873>
- Counts, J.W., Jorry, S.J., Vazquez-Riveiros, N., Amy, L.A., Dennielou, E., Jouet, G., 2021. Sedimentology and distribution of late quaternary calciturbidites and calcidebrites in the Mozambique Channel (Southwest Indian Ocean). *Facies* 67, 17. <https://doi.org/10.1007/s10347-021-00624-1>
- Counts, J.W., Jorry, S.J., Vazquez Riveiros, N., Jouet, G., Giraudeau, J., Cheron, S., Boissier, A., Miramontes, E., 2019. A Late Quaternary record of highstand shedding from an isolated carbonate platform (Juan de Nova, southern Indian Ocean). *Depos. Rec.* 5, 540–557. <https://doi.org/10.1002/dep2.57>
- de Menocal, P.B., 2015. End of the African Humid Period. *Nat. Geosci.* 8, 86–87. <https://doi.org/10.1038/ngeo2355>
- deMenocal, P., Ortiz, J., Guilderson, T., Adkins, J., Sarnthein, M., Baker, L., Yarusinsky, M., 2000. Abrupt onset and termination of the African Humid Period: *Quat. Sci. Rev.* 19, 347–361. [https://doi.org/10.1016/S0277-3791\(99\)00081-5](https://doi.org/10.1016/S0277-3791(99)00081-5)
- Dix, G.R., Mullins, H.T., 1988a. Rapid burial diagenesis of deep-water carbonates: Exuma Sound, Bahamas. *Geology* 16, 680. [https://doi.org/10.1130/0091-7613\(1988\)016<0680:RBDODW>2.3.CO;2](https://doi.org/10.1130/0091-7613(1988)016<0680:RBDODW>2.3.CO;2)
- Dix, G.R., Mullins, H.T., 1988b. A regional perspective of shallow-burial diagenesis of deep-water periplatform carbonates from the northern Bahamas. *Proc., Sci. results, ODP, Leg 101, Bahamas 101*, 279–302. <https://doi.org/10.2973/odp.proc.sr.101.132.1988>
- Droxler, A.W., Schlager, W., Whallon, C.C., 1983. Quaternary aragonite cycles and oxygen-isotope record in Bahamian carbonate ooze. *Geology* 11, 235. [https://doi.org/10.1130/0091-7613\(1983\)11<235:QACAOR>2.0.CO;2](https://doi.org/10.1130/0091-7613(1983)11<235:QACAOR>2.0.CO;2)
- Dunbar, G.B., Dickens, G.R., 2003. Late Quaternary shedding of shallow-marine carbonate along a tropical mixed siliciclastic-carbonate shelf: Great Barrier Reef, Australia.
- Bialik et al., Mesophotic post-glacial carbonate-platform export patterns

- Sedimentology 50, 1061–1077. <https://doi.org/10.1046/j.1365-3091.2003.00593.x>
- Duncan, R.A., Hargraves, R.B., 1990. $^{40}\text{Ar}/^{39}\text{Ar}$ geochronology of basement rocks from the Mascarene Plateau, the Chagos Bank, and the Maldives Ridge. Proc., Sci. results, ODP, Leg 115, Mascarene Plateau 115, 43–51.
<https://doi.org/10.2973/odp.proc.sr.115.141.1991>
- Dunham, R.J., 1962. Classification of Carbonate Rocks According to Depositional Textures, in: Ham, W.E. (Ed.), Classification of Carbonate Rocks - A Symposium. AAPG Memoir 1, pp. 108–121.
- Eberli, G.P., Swart, P.K., Malone, M.J., 1997a. Site 1006. Proc. Ocean Drill. Program, Initial Reports Vol. 166 166, 161–165.
- Eberli, G.P., Swart, P.K., McNeill, D.F., Kenter, J.A.M., Anselmetti, F.S., Melim, L.A., Ginsburg, R.N., 1997b. A Synopsis of the Bahamas Drilling Project: Results from Two Deep Core Borings Drilled on the Great Bahama Bank, in: Eberli, G. P., Swart, P.K., Malone, M.J. (Eds.), Proceedings of the Ocean Drilling Program, 166 Initial Reports. Ocean Drilling Program, V. 166, pp. 23–41.
<https://doi.org/10.2973/odp.proc.ir.166.103.1997>
- Emmermann, P., 2000. Mineralogy , geochemistry and microfacies of late Quaternary periplatform sediments : Carbonate export cycles and secondary processes - Sanganeb Atoll and Abington Reef , Sudan , Central Red Sea. Christian-Albrechts-Universität Keil.
- Fantle, M.S., DePaolo, D.J., 2007. Ca isotopes in carbonate sediment and pore fluid from ODP Site 807A: The $\text{Ca}^{2+}(\text{aq})$ –calcite equilibrium fractionation factor and calcite recrystallization rates in Pleistocene sediments. Geochim. Cosmochim. Acta 71, 2524–2546. <https://doi.org/10.1016/j.gca.2007.03.006>
- Fedorov, V. V., Rubinshteyn, I.G., Danilov, I. V., Ianin, V.I., 1980. Bottom landscape of the Saya de Malha bank in the Indian Ocean. Oceanology 20, 434–439.
- Fisher, R.L., Johnson, G.L., Cheezen, B.C., 1967. Mascarene Plateau, Western Indian Ocean. GSA Bull. 78, 1247–1266. [https://doi.org/10.1130/0016-7606\(1967\)78\[1247:MPWIO\]2.0.CO;2](https://doi.org/10.1130/0016-7606(1967)78[1247:MPWIO]2.0.CO;2)
- Folk, R.L., Ward, W.C., 1957. Brazos River bar [Texas]; a study in the significance of grain size parameters. J. Sediment. Res. 27, 3–26. <https://doi.org/10.1306/74D70646-2B21-11D7-8648000102C1865D>
- Gaye, B., Böll, A., Segschneider, J., Burdanowitz, N., Emeis, K.-C., Ramaswamy, V.,
- Bialik et al., Mesophotic post-glacial carbonate-platform export patterns

- Lahajnar, N., Lückge, A., Rixen, T., 2018. Glacial–interglacial changes and Holocene variations in Arabian Sea denitrification. *Biogeosciences* 15, 507–527.
<https://doi.org/10.5194/bg-15-507-2018>
- Gischler, E., Zingeler, D., 2002. The origin of carbonate mud in isolated carbonate platforms of Belize, Central America. *Int. J. Earth Sci.* 91, 1054–1070.
<https://doi.org/10.1007/s00531-002-0288-5>
- Gourlan, A.T., Meynadier, L., Allègre, C.J., 2008. Tectonically driven changes in the Indian Ocean circulation over the last 25 Ma: Neodymium isotope evidence. *Earth Planet. Sci. Lett.* 267, 353–364. <https://doi.org/10.1016/j.epsl.2007.11.054>
- Grossowicz, M., Benayahu, Y., 2015. Occurrence and survivorship of azooxanthellate octocorals reflect recruitment preferences and depth distribution. *Hydrobiologia* 759, 85–93. <https://doi.org/10.1007/s10750-015-2270-9>
- Heaton, T.J., Köhler, P., Butzin, M., Bard, E., Reimer, R.W., Austin, W.E.N., Bronk Ramsey, C., Grootes, P.M., Hughen, K.A., Kromer, B., Reimer, P.J., Adkins, J., Burke, A., Cook, M.S., Olsen, J., Skinner, L.C., 2020. Marine20—The Marine Radiocarbon Age Calibration Curve (0–55,000 cal BP). *Radiocarbon* 62, 779–820.
<https://doi.org/10.1017/RDC.2020.68>
- Jorry, S.J., Camoin, G.F., Jouet, G., Roy, P. Le, Vella, C., Courgeon, S., Prat, S., Fontanier, C., Paumard, V., Boule, J., Caline, B., Borgomano, J., 2016. Modern sediments and Pleistocene reefs from isolated carbonate platforms (Iles Eparses, SW Indian Ocean): A preliminary study. *Acta Oecologica* 72, 129–143.
<https://doi.org/10.1016/j.actao.2015.10.014>
- Jorry, S.J., Jouet, G., Edinger, E.N., Toucanne, S., Counts, J.W., Miramontes, E., Courgeon, S., Vázquez, N., Le, P., Camoin, G.F., 2020. From platform top to adjacent deep sea : New source-to-sink insights into carbonate sediment production and transfer in the SW Indian Ocean (Glorieuses archipelago). *Mar. Geol.* 423, 106144.
<https://doi.org/10.1016/j.margeo.2020.106144>
- Kleypas, J.A., 1997. Modeled estimates of global reef habitat and carbonate production since the Last Glacial Maximum. *Paleoceanography* 12, 533–545.
<https://doi.org/10.1029/97PA01134>
- Kok, J.F., Adebisi, A.A., Albani, S., Balkanski, Y., Checa-Garcia, R., Chin, M., Colarco, P.R., Hamilton, D.S., Huang, Y., Ito, A., Klose, M., Li, L., Mahowald, N.M., Miller, R.L., Obiso, V., Pérez García-Pando, C., Rocha-Lima, A., Wan, J.S., 2021. Contribution of the
- Bialik et al., Mesophotic post-glacial carbonate-platform export patterns

- world's main dust source regions to the global cycle of desert dust. *Atmos. Chem. Phys.* 21, 8169–8193. <https://doi.org/10.5194/acp-21-8169-2021>
- Lantzsch, H., Roth, S., Reijmer, J.J.G., Kinkel, H., 2007. Sea-level related re-sedimentation processes on the northern slope of Little Bahama Bank (Middle Pleistocene to Holocene). *Sedimentology* 54, 1307–1322. <https://doi.org/10.1111/j.1365-3091.2007.00882.x>
- Léon, J.-F., Legrand, M., 2003. Mineral dust sources in the surroundings of the north Indian Ocean. *Geophys. Res. Lett.* 30. <https://doi.org/10.1029/2002GL016690>
- Lindhorst, S., 2019. Short Cruise Report RV SONNE SO270. Hamburg.
- Lindhorst, S., Appoo, J., Artschwager, M., Bialik, O., Birkicht, M., Bissessur, D., Braga, J.-C., Budke, L., Bunzel, D., Coopen, P., Eberhardt, B., Eggers, D., Eisermann, J.O., El Gareb, F., Emeis, K., Geßner, A.-L., Hüge, F., Knaack-Völker, H., Kornrumpf, N., Lenz, N., Lüdmann, T., Metzke, M., Naderipour, C., Neziraj, G., Reijmer, J., Reolid, J., Reule, N., Rixen, T., Saitz, Y., Schäfer, W., Schutter, I., Siddiqui, C., Sorry, A., Taphorn, B., Vosen, S., Wasilewski, T., Welsch, A., 2019. Saya de Malha Carbonates, Oceanography and Biogeochemistry (Western Indian Ocean) Cruise No. SO270, 2019-09-06 - 2019-10-23, Hong Kong (China) - Port Louis (Mauritius). SONNE-Berichte, SO270. Gutachterpanel Forschungsschiffe, Bonn. https://doi.org/10.2312/cr_so270
- Lisiecki, L.E., Raymo, M.E., 2005. A Pliocene-Pleistocene stack of 57 globally distributed benthic $\delta^{18}O$ records. *Paleoceanography* 20, 1–17. <https://doi.org/10.1029/2004PA001071>
- Mavume, A., Rydberg, L., Rouault, M., Lutjeharms, J., 2010. Climatology and Landfall of Tropical Cyclones in the South- West Indian Ocean. *West. Indian Ocean J. Mar. Sci.* 8. <https://doi.org/10.4314/wiojms.v8i1.56672>
- Melim, L., Westphal, H., Swart, P., Eberli, G., Munnecke, a, 2002. Questioning carbonate diagenetic paradigms: evidence from the Neogene of the Bahamas. *Mar. Geol.* 185, 27–53. [https://doi.org/10.1016/S0025-3227\(01\)00289-4](https://doi.org/10.1016/S0025-3227(01)00289-4)
- Meyerhoff, A.A., Kamen-Kaye, M., 1981. Petroleum Prospects of Saya de Malha and Nazareth Banks, Indian Ocean. *Am. Assoc. Pet. Geol. Bull.* 65, 1344–1347. <https://doi.org/10.1306/03B594AE-16D1-11D7-8645000102C1865D>
- Milliman, J.D., Freile, D., Steinen, R.P., Wilber, R.J., 1993. Great-Bahama Bank aragonitic muds; mostly inorganically precipitated, mostly exported. *J. Sediment. Res.* 63, 589–595.
- Bialik et al., Mesophotic post-glacial carbonate-platform export patterns

- Mullins, H.T., Wise, S.W., Gardulski, A.F., Hinchey, E.J., Masters, P.M., Siegel, D.I., 1985. Shallow subsurface diagenesis of Pleistocene periplatform ooze: northern Bahamas. *Sedimentology* 32, 473–494. <https://doi.org/10.1111/j.1365-3091.1985.tb00465.x>
- Murtugudde, R., Seager, R., Thoppil, P., 2007. Arabian Sea response to monsoon variations. *Paleoceanography* 22, n/a-n/a. <https://doi.org/10.1029/2007PA001467>
- New, A.L., Stansfield, K., Smythe-Wright, D., Smeed, D.A., Evans, A.J., Alderson, S.G., 2005. Physical and biochemical aspects of the flow across the Mascarene Plateau in the Indian Ocean. *Philos. Trans. R. Soc. A Math. Phys. Eng. Sci.* 363, 151–168. <https://doi.org/10.1098/rsta.2004.1484>
- Nohl, T., Jarochovska, E., Munnecke, A., 2018. Revealing the genesis of limestone-marl alternations: a taphonomic approach. *Palaios* 34, 15–31. <https://doi.org/10.2110/palo.2018.062>
- Nohl, T., Steinbauer, M.J., Sinnesael, M., Jarochovska, E., 2021. Detecting initial aragonite and calcite variations in limestone–marl alternations. *Sedimentology* 68, 3102–3115. <https://doi.org/10.1111/sed.12885>
- Paul, A., Reijmer, J.J.G., Fürstenau, J., Kinkel, H., Betzler, C., 2012. Relationship between Late Pleistocene sea-level variations, carbonate platform morphology and aragonite production (Maldives, Indian Ocean). *Sedimentology* 59, 1640–1658. <https://doi.org/10.1111/j.1365-3091.2011.01319.x>
- Perrin, C., Bosence, D., Rosen, B., 1995. Quantitative approaches to palaeozonation and palaeobathymetry of corals and coralline algae in Cenozoic reefs. *Geol. Soc. London, Spec. Publ.* 83, 181–229. <https://doi.org/10.1144/GSL.SP.1995.083.01.10>
- Poli, M.S., Meyers, P.A., Thunell, R.C., 2010. The western North Atlantic record of MIS 13 to 10: Changes in primary productivity, organic carbon accumulation and benthic foraminiferal assemblages in sediments from the Blake Outer Ridge (ODP Site 1058). *Palaeogeogr. Palaeoclimatol. Palaeoecol.* 295, 89–101. <https://doi.org/10.1016/j.palaeo.2010.05.018>
- Pratson, L.F., Imran, J., Parker, G., Syvitski, J.P.M., Hutton, E., 2000. Debris Flows vs. Turbidity Currents: a Modeling Comparison of Their Dynamics and Deposits. *Fine-Grained Turbid. Syst.* <https://doi.org/10.1306/M72703C6>
- Prell, W.L., 1984. Variation of monsoonal upwelling: A response to changing solar radiation, in: Hansen, J.E., Takahashi, T. (Eds.), *Climate Processes and Climate Sensitivity*, Volume 29. American Geophysical Union, Geophysical Monograph Series, pp. 48–57.
- Bialik et al., Mesophotic post-glacial carbonate-platform export patterns

<https://doi.org/10.1029/GM029p0048>

- Prell, W.L., Campo, E. Van, 1986. Coherent response of Arabian Sea upwelling and pollen transport to late Quaternary monsoonal winds. *Nature* 323, 526–528.
<https://doi.org/10.1038/323526a0>
- Rathbun, M.J., 1911. Reports of the Percy Sladen Trust Expedition to the Indian Ocean in 1905, under the leadership of Mr. J. Stanley Gardiner. *Mar. Brachyura* 3, 191--261.
- Raymo, M.E., Ruddiman, W.F., Shackleton, N.J., Oppo, D.W., 1990. Evolution of Atlantic-Pacific $\delta^{13}\text{C}$ gradients over the last 2.5 m.y. *Earth Planet. Sci. Lett.* 97, 353–368.
[https://doi.org/10.1016/0012-821X\(90\)90051-X](https://doi.org/10.1016/0012-821X(90)90051-X)
- Reijmer, J.J.G., Schlager, W., Droxler, A.W., 1988. Site 632: Pliocene-Pleistocene sedimentation cycles in a Bahamian basin, in: *Proceedings of the Ocean Drilling Program, Scientific Results - Part B, ODP. International Ocean Discovery Program, College Station, USA*, pp. 213–220.
- Reijmer, J.J.G.G., Andresen, N., 2007. Mineralogy and grain size variations along two carbonate margin-to-basin transects (Pedro Bank, Northern Nicaragua Rise). *Sediment. Geol.* 198, 327–350. <https://doi.org/10.1016/j.sedgeo.2007.01.018>
- Ren, J., Jiang, H., Seidenkrantz, M.-S., Kuijpers, A., 2009. A diatom-based reconstruction of Early Holocene hydrographic and climatic change in a southwest Greenland fjord. *Mar. Micropaleontol.* 70, 166–176. <https://doi.org/10.1016/j.marmicro.2008.12.003>
- Rendle, R.H., Reijmer, J.J.G., Kroon, D., Henderson, G.M., 2000. Mineralogy and sedimentology of the Pleistocene to Holocene on the leeward margin of Great Bahama Bank. *Proc. Ocean Drill. Progr. Sci. Results* 166, 61–76.
<https://doi.org/10.2973/odp.proc.sr.166.114.2000>
- Reuning, L., Reijmer, J.J.G., Mattioli, E., 2006. Aragonite cycles: diagenesis caught in the act. *Sedimentology* 53, 849–866. <https://doi.org/10.1111/j.1365-3091.2006.00799.x>
- Rohling, E.J., Cane, T.R., Cooke, S., Sprovieri, M., Bouloubassi, I., Emeis, K.C., Schiebel, R., Kroon, D., Jorissen, F.J., Lorre, a., Kemp, a. E.S., 2002. African monsoon variability during the previous interglacial maximum. *Earth Planet. Sci. Lett.* 202, 61–75.
[https://doi.org/10.1016/S0012-821X\(02\)00775-6](https://doi.org/10.1016/S0012-821X(02)00775-6)
- Rohling, E.J., Marino, G., Grant, K.M., 2015. Mediterranean climate and oceanography, and the periodic development of anoxic events (sapropels). *Earth-Science Rev.* 143, 62–97.
<https://doi.org/10.1016/j.earscirev.2015.01.008>

- Schlager, W., 2003. Benthic carbonate factories of the Phanerozoic. *Int. J. Earth Sci.* 92, 445–464. <https://doi.org/10.1007/s00531-003-0327-x>
- Schlager, W., Reijmer, J.J.G., Droxler, A., 1994. Highstand Shedding of Carbonate Platforms. *J. Sediment. Res.* B64, 270–281. <https://doi.org/10.1306/D4267FAA-2B26-11D7-8648000102C1865D>
- Shipboard Scientific Party, 1997. Site 1003, in: Eberli, G.P., Swart, P.K., Malone, M. (Eds.), *Proceedings of the Ocean Drilling Program, 166 Initial Reports. Ocean Drilling Program, Vol 166*, pp. 71–151. <https://doi.org/10.2973/odp.proc.ir.166.106.1997>
- Sirisha, P., Remya, P.G., Balakrishnan Nair, T.M., Rao, B.V., 2015. Numerical simulation and observations of very severe cyclone generated surface wave fields in the north Indian Ocean. *J. Earth Syst. Sci.* 124, 1639–1651. <https://doi.org/10.1007/s12040-015-0637-y>
- Sisma-Ventura, G., Bialik, O.M., Yam, R., Herut, B., Silverman, J., 2017. pCO₂ variability in the surface waters of the ultra-oligotrophic Levantine Sea: Exploring the air-sea CO₂ fluxes in a fast warming region. *Mar. Chem.* <https://doi.org/10.1016/j.marchem.2017.06.006>
- Slowey, N.C., Wilber, R.J., Haddad, G.A., Henderson, G.M., 2002. Glacial-to-Holocene sedimentation on the western slope of Great Bahama Bank. *Mar. Geol.* 185, 165–176. [https://doi.org/10.1016/S0025-3227\(01\)00295-X](https://doi.org/10.1016/S0025-3227(01)00295-X)
- Spratt, R.M., Lisiecki, L.E., 2016. A Late Pleistocene sea level stack. *Clim. Past* 12, 1079–1092. <https://doi.org/10.5194/cp-12-1079-2016>
- Spratt, R.M., Lisiecki, L.E., 2015. A Late Pleistocene sea level stack. *Clim. Past Discuss.* 11, 3699–3728. <https://doi.org/10.5194/cpd-11-3699-2015>
- Sulpis, O., Agrawal, P., Wolthers, M., Munhoven, G., Walker, M., Middelburg, J.J., 2022. Aragonite dissolution protects calcite at the seafloor. *Nat. Commun.* 13, 1104. <https://doi.org/10.1038/s41467-022-28711-z>
- Sulpis, O., Jeansson, E., Dinauer, A., Lauvset, S.K., Middelburg, J.J., 2021. Calcium carbonate dissolution patterns in the ocean. *Nat. Geosci.* 14, 423–428. <https://doi.org/10.1038/s41561-021-00743-y>
- Swart, P.K., Guzikowski, M., 1988. Interstitial-water chemistry and diagenesis of periplatform sediments from the Bahamas, ODP Leg 101. *Proc., Sci. results, ODP, Leg 101, Bahamas 101*, 363–380. <https://doi.org/10.2973/odp.proc.sr.101.158.1988>

- Swart, P.K., Mackenzie, G.J., Eberli, G.P., Lüdmann, T., Betzler, C., 2019. Do drifts deposited adjacent to carbonate platforms record the signal of global carbon isotopic values? *Sedimentology*. <https://doi.org/10.1111/sed.12580>
- Swart, P.K., Oehlert, A.M., Mackenzie, G.J., Eberli, G.P., Reijmer, J.J.G., 2014. The fertilization of the Bahamas by Saharan dust: A trigger for carbonate precipitation? *Geology* 42, 671–674. <https://doi.org/10.1130/G35744.1>
- Travin, V.I., 1968. Science-trade investigations AzCherNIRO in north-west region of Indian Ocean. *VNIRO* 64, 25.
- Turpin, M., Emmanuel, L., Reijmer, J.J.G., Renard, M., 2011. Whiting-related sediment export along the Middle Miocene carbonate ramp of Great Bahama Bank. *Int. J. Earth Sci.* 100, 1875–1893. <https://doi.org/10.1007/s00531-010-0627-x>
- Vortsepneva, E., 2008. Saya de Malha Bank – an invisible island in the Indian Ocean. Moscow, Russia.
- Yesson, C., Taylor, M.L., Tittensor, D.P., Davies, A.J., Guinotte, J., Baco, A., Black, J., Hall-Spencer, J.M., Rogers, A.D., 2012. Global habitat suitability of cold-water octocorals. *J. Biogeogr.* 39, 1278–1292. <https://doi.org/10.1111/j.1365-2699.2011.02681.x>
- Zhao, Y., Braconnot, P., Marti, O., Harrison, S.P., Hewitt, C., Kitoh, A., Liu, Z., Mikolajewicz, U., Otto-Bliesner, B., Weber, S.L., 2005. A multi-model analysis of the role of the ocean on the African and Indian monsoon during the mid-Holocene. *Clim. Dyn.* 25, 777–800. <https://doi.org/10.1007/s00382-005-0075-7>
- Ziegler, M., Tuenter, E., Lourens, L.J., 2010. The precession phase of the boreal summer monsoon as viewed from the eastern Mediterranean (ODP Site 968). *Quat. Sci. Rev.* 29, 1481–1490. <https://doi.org/10.1016/j.quascirev.2010.03.011>
- Zirks, E., Krom, M.D., Zhu, D., Schmiedl, G., Goodman-Tchernov, B.N., 2019. Evidence for the Presence of Oxygen-Depleted Sapropel Intermediate Water across the Eastern Mediterranean during Sapropel S1. *ACS Earth Sp. Chem.* 3, 2287–2297. <https://doi.org/10.1021/acsearthspacechem.9b00128>